Modification of Nanodiamonds by Xenon Implantation: A Molecular Dynamics Study

Jason L. Fogg[a], Alireza Aghajamali[a], Jonathan A. Hinks[b], Stephen E. Donnelly[b], Andrey. A. Shiryaev[c], Nigel A. Marks[a,*]

[a]*Department of Physics and Astronomy, Curtin University, Perth WA 6102, Australia*
[b]*University of Huddersfield, Queensgate, Huddersfield, HD1 3DH, United Kingdom*
[c]*Frumkin Institute of Physical Chemistry and Electrochemistry RAS, Leninsky pr .31 korp. 4, Moscow, 119071, Russia*

Abstract

Xenon implantation into nanodiamonds is studied using molecular dynamics. The nanodiamonds range in size from 2–10 nm and the primary knock-on (PKA) energy extends up to 40 keV. For small nanodiamonds an energy-window effect occurs in which PKA energies of around 6 keV destroy the nanodiamond, while in larger nanodiamonds the radiation cascade is increasingly similar to those in bulk material. Destruction of the small nanodiamonds occurs due to thermal annealing associated with the small size of the particles and the absence of a heat-loss path. Simulations are also performed for a range of impact parameters, and for a series of double-nanodiamond systems in which a heat-loss path is present. The latter show that the thermal shock caused by the impact occurs on the timescale of a few picoseconds. These findings are relevant to ion-beam modification of nanoparticles by noble gases as well as meteoritic studies where implantation is proposed as the mechanism for xenon incorporation in pre-solar nanodiamonds.

Keywords: Nanodiamonds, Xenon, Molecular Dynamics, Ion Implantation

1. Introduction

Nanodiamonds are found in primitive chondritic meteorites at concentrations as high as 1500 ppm [1]. Within these nanodiamonds (NDs) are trace amounts of xenon and other noble gases whose unusual isotopic abundances indicate a pre-solar origin and provide information on nucleosynthesis processes in supernovae. Ion-implantation is the most popular explanation for the presence of the noble gases in NDs [2, 3, 4, 5], although another possibility is that the noble gases were incorporated during growth of the ND. The implantation hypothesis was studied experimentally by Koscheev et al. [6] and Verchovsky et al. [7] using low-energy implantation into detonation nanodiamonds, which are similar in size to meteoritic NDs. Even though their studies employed only a single implantation energy and used isotopes of natural abundance, many of the characteristics observed in the meteoritic data were observed.

Recently we performed a combined experimental and computational study of xenon implantation into nanodiamonds of varying size [8]. Implantation experiments were performed *in situ* in a transmission electron microscope (TEM), enabling real-time monitoring of irradiation effects. While large NDs (40 nm diameter) were resistant to the ion beam, the small NDs (2–3 nm) were gradually destroyed under 6 keV irradiation. SRIM calculations do not predict this effect, while Molecular Dynamics (MD) simulations explained these observations via a temperature effect, which anneals the smaller-sized NDs. The success of the MD approach is that it goes beyond the binary-collision approximation used by SRIM, and captures all the thermal motion associated with the collision cascade.

In this work our MD studies of xenon implantation into ND is extended in two main ways: (i) low implantation energies are considered to study the hypothesis explored by Koscheev et al. [6] and Verchovsky et al. [7], and (ii) a second ND particle is introduced to capture thermal conduction effects relevant to the *in situ* experiments. We also examine the effect of varying the impact parameter and include a comprehensive description of the simulation approach, including the description of the Xe–C interactions and the methodology for generating the ND coordinates. The latter is a useful starting point for further investigations of noble gases within nanodiamonds.

The simulations are performed using the environment dependent interaction potential [9, 10] which provides an excellent description of both sp^2 (graphite) and sp^3 (diamond) bonding [11]. A large number of primary knock-on atom (PKA) directions and energies are used to collect a statistically significant data set. The nanodiamonds vary in size from 2 and 10 nm, and PKA energies from 50 eV up to 40 keV are considered.

2. Methodology

Atomic interactions between carbon atoms were described using the environment dependent interaction potential (EDIP) for carbon, coupled with the Ziegler-Biersack-Littmark (ZBL) potential [12] for close interactions. This combination has been previously been successfully employed to model radiation damage cascades in graphite [13, 14] and diamond [15]. Full details of the interpolation process used to switch between the EDIP and ZBL forms is provided in Ref. [13]. The EDIP functional form provides an excellent description of the competing hybridizations in carbon, in particular the energy barrier between graphite and diamond. In a recent comparison of carbon

*Corresponding author. N.Marks@curtin.edu.au

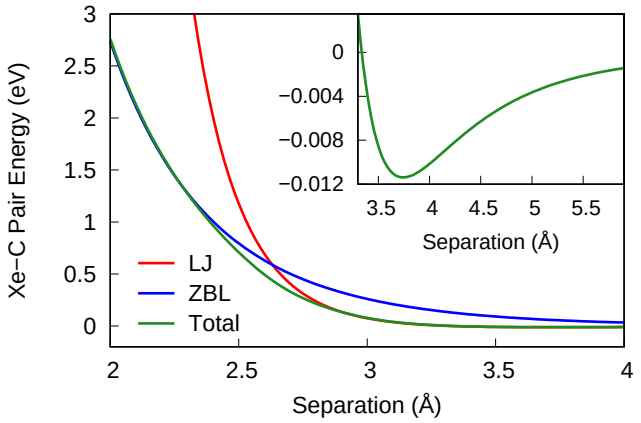

Figure 1: Interaction energy between the Xe and carbon atoms (green line). At close approach the interaction is pure ZBL (blue line), while at distances around equilibrium and greater a Lennard-Jones (LJ) expression is used (red line). Interpolation at intermediate distances is performed using a Fermi-like switching function as described in the text.

potentials [11], we found that EDIP has excellent transferability across a wide range of conditions, and is superior to many common carbon potentials. One aspect of EDIP which is still being developed is the ability to describe hydrogen, and hence all nanodiamonds in the simulations are dehydrogenated.

For the Xe-C interactions, we used the standard ZBL potential coupled with a Lennard-Jones potential of the form

$$U(r) = 4\varepsilon_{\mathrm{Xe-C}}\left\{\left(\frac{\sigma_{\mathrm{Xe-C}}}{r}\right)^{12} - \left(\frac{\sigma_{\mathrm{Xe-C}}}{r}\right)^{6}\right\}$$

with parameters $\varepsilon_{\mathrm{Xe-C}}$=0.0114 eV and $\sigma_{\mathrm{Xe-C}}$=3.332 Å as given in Ref. [16]. For simplicity, we did not employ the anistropic terms as implemented in Ref. [16]. Interpolation between the LJ form and the ZBL interaction was described in the same manner as Refs. [13, 15], using Fermi-type switching functions. The parameters were empirically determined to provide a smooth transition from the strong repulsive region of the ZBL to the weakly attractive region of the LJ potential. The resulting functional form of the energy for Xe-C interactions was

$$U(r) = U_{\mathrm{ZBL}}(r) \times f(r+\delta) + U_{\mathrm{LJ}}(r) \times (1 - f(r-\delta))$$

where δ=0.07 Å and

$$f(r) = \left[1 + \exp\left(8 \times (r - 2.7)\right)\right]^{-1}.$$

A plot of the Xe-C interaction energy covering the ZBL and LJ regimes is shown in Fig. 1, with the attractive region shown in the inset.

The simulations were performed using an in-house Molecular Dynamics package developed by one of the authors (NAM). All calculations were performed in an NVE ensemble (constant number of particles, volume and energy), using Verlet integration and a variable timestep [17]. The algorithm for the timestep automatically adjusts the timestep using the metric $||\mathbf{F}_{\mathrm{max}}||\Delta t$ as described in detail in Ref. [17]. During close approaches the timestep was reduced to values as small as 10^{-5} fs, and was subsequently increased as kinetic energy was dispersed and the system equilibrated. Periodic boundary conditions were not employed. Prior to implantation, all nanodiamond coordinates were relaxed by steepest descent and equilibrated at 300 K. The majority of the simulations were 1 ps in length, which was sufficient to model the ballistic phase of the Xe implantation onto the nanodiamond. A smaller number of longer simulations extending up to 85 ps were performed to study annealing effects and thermal transport. Visualization was performed using the OVITO software [18] and a cutoff of 1.85 Å was to determine the coordination number. Temperatures were determined using the kinetic energy of the main carbon cluster; the xenon atom and any ejected carbon atoms were excluded from the calculation and the net momentum of the cluster was subtracted prior to computing the temperature.

Construction of the nanodiamond coordinates is a non-trivial problem. The question of stable nanodiamond morphologies has been extensively studied by Barnard and Zapol, [19] and some sets of Cartesian coordinates are available online [20]. For dehydrogenated nanodiamonds, they showed that the relevant stable geometry is the truncated octahedron, formed by cleaving a carbon nanoparticle out of diamond such that it has only 100 and 111 faces (see Fig. 8 in Ref [19]). One important detail of dehydrogenated nanodiamonds is that the 100 surfaces need to be reconstructed in a 2×1 arrangement to eliminate dangling bonds (two-fold coordinated atoms) on the 100 surface. All of these aspects were implemented in a Fortran program which is available on request. The program generates a nanodiamond of arbitrary size, with all atoms at the surface being sp^2 bonded (the 100 surface due to the reconstruction, and the 111 surface by design). Table 1 lists all of the NDs studied in this work; the parameters d_{100} and d_{111} are the distances from the origin to the 100 and 111 planes, respectively. The radius was measured by computing the average distance between sp^2 bonded atoms and the centre-of-mass of the ND. The NDs studied in this work span the typical range observed for meteoritic ND (range of 1–10 nm, with average diameter of around 3 nm; Ref. [1, 21]) and detonation ND (average of 4–5 nm).

Table 1: Parameters (number of atoms and distances), diameter and sp^3 fraction for the twelve NDs studied in this work.

Diameter (nm)	N_{atoms}	d_{111} (Å)	d_{100} (Å)	sp^3 (%)
2.1	837	9	10	69.9
2.6	1639	12	14	74.9
3.1	2793	14	17	78.4
3.6	4363	15	21	81.0
4.0	5975	18	21	83.7
4.6	8389	20	24	85.4
5.1	11591	22	27	86.6
6.0	18977	26	31	88.8
7.1	29359	30.5	35.5	90.4
8.0	46393	35	46	91.3
9.0	61849	39	46	92.4
10.2	90395	44	49	93.5

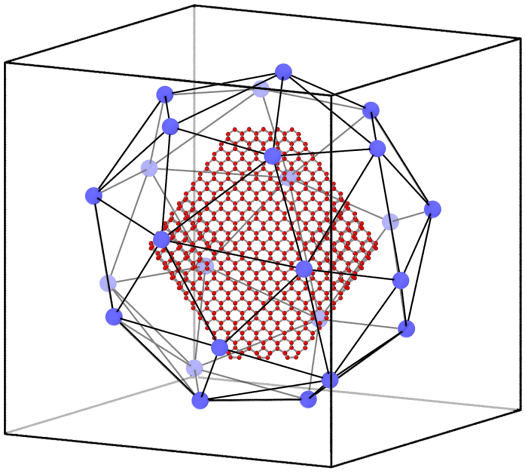

Figure 2: Schematic showing the typical geometric relationship between a ND and the initial PKA locations. The ND atoms are shown in red, and in this example a 4.0 nm diameter ND is shown. The PKA locations (shown in blue) are solutions to the 25-point Thomson problem. When the PKA is initiated, the Xe travels towards the centre of the ND. For calculations studying the effect of impact parameter, the ND is offset as described in the text.

Our largest ND of 10 nm is of sufficient size to exhibit bulk-like behaviour, and hence we did not simulate the 40 nm diamonds studied in Ref. [8].

The energy of the implanting xenon, which for brevity we refer to as the primary knock-on atom (PKA), was varied between 2 and 40 keV, with most simulations performed using 6 keV. The initial position of the PKA was always 5 Å beyond the edge of the ND and for most simulations the initial velocity vector was towards the centre of the ND. In a small number of simulations (see Supplementary Material) the ND was displaced perpendicular to the initial velocity vector to study the effect of varying the impact parameter. The result was as intuitively expected; namely that a higher impact parameter progressively transfers less energy to the ND, tending to zero effect when the Xe grazes the edge of the ND. To collect robust statistics across the various crystallographic orientations, the xenon atom was introduced at 25 different locations distributed uniformly around the ND. A schematic indicating a ND and the various xenon positions is shown in Fig. 2 and Supplementary Movie S1; note that the location of the xenon atoms has been expanded outwards for clarity. The 25 points shown are solutions to the Thomson problem [22], an exercise in mathematical optimization in which point charges repel each other on the unit sphere. For further examples of the usefulness of the Thomson problem and its applicability to radiation damage simulations, see Refs. [13, 15, 23, 24, 25].

3. Results

The implantation of a xenon atom into the ND is a highly energetic event, leading to substantial disruption in certain cases. Figs. 3 and 4 show representative implantations for varying PKA energies incident onto a 3.1 nm diameter ND. In each case the initial position and velocity vector is the same; Fig. 3 plots the time-variation of the cluster temperature and sp^3 fraction, while Fig. 4 shows a series of snapshots. Note that the cluster temperature refers only to carbon atoms retained within the cluster, with the xenon and any ejected carbon atoms excluded from the calculation. Video animation sequences of all three impacts are provided in the Supplementary Material.

At 2 keV the Xe atom deposits almost all of its kinetic energy into the ND. As shown in the top panel of Fig. 4, the Xe takes 0.2 ps to travel through the ND, ejecting a small number of carbon atoms (six) in the process. For the case shown, the Xe exits the ND with just 24 eV of energy, while for other PKA directions the Xe end-of-range sometimes falls within the ND. The transfer of kinetic energy into the ND rapidly increases the temperature of the ND, as shown in Fig. 3(a); after a very short period (less than 0.1 ps) the temperature reaches equilibrium at a value slightly above 2000 K. This temperature is sufficient to slightly reduce the number of sp^3 bonds [Fig. 3(b)] in the ND, principally at the 111 edges on the right-hand side of the ND where a small amount of graphitization occurs. Figure 3(b) also shows that for the 2 keV impact the sp^3 fraction undergoes oscillations which gradually die away; these reflect a "ringing" of the structure in which sound waves reflect back-and-forth across the ND.

The bottom panel of Fig. 4 shows that implantation of a 40 keV Xe has a similar effect on the ND as seen at 2 keV. The

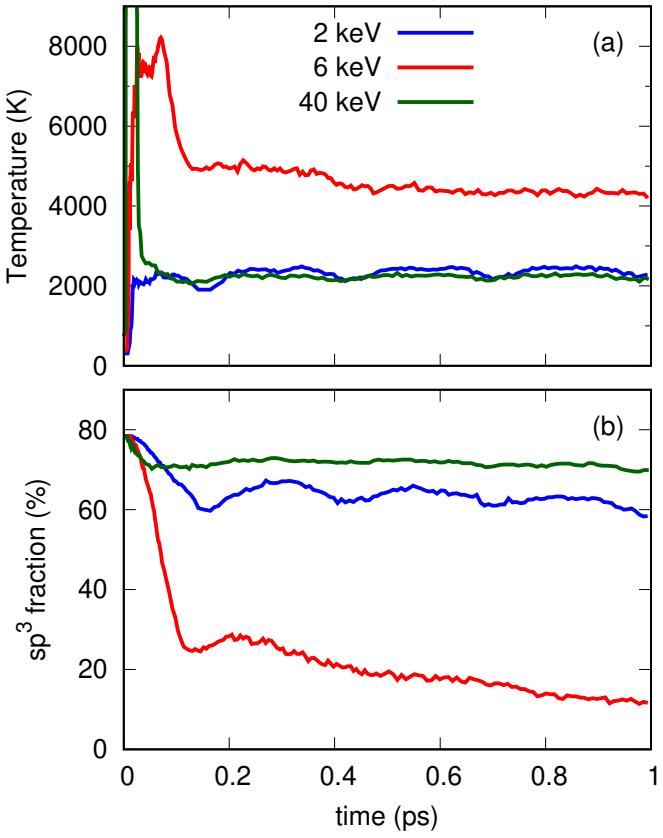

Figure 3: Time evolution of the cluster temperature [panel (a)] and sp^3 fraction [panel (b)] for the three xenon implantation events shown in Fig. 4.

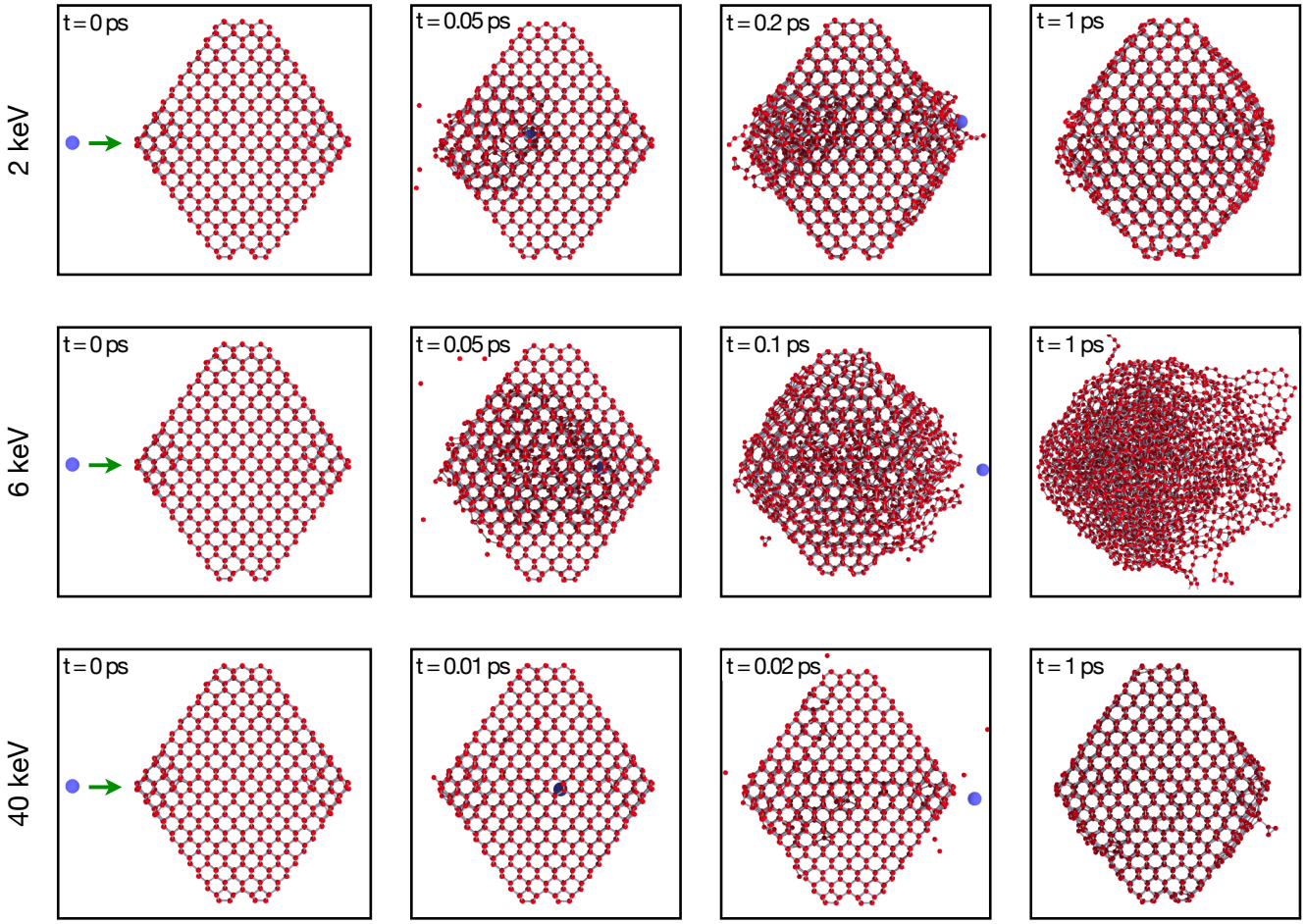

Figure 4: Time evolution of a three typical implantation events into a 3.1 nm diameter nanodiamond for PKA energies of 2, 6 and 40 keV. In each case the Xe PKA exits the nanodiamond. Only at 6 keV is there any significant destruction of the nanodiamond. Carbon atoms and the xenon are shown as red and blue circles respectively.

chief difference is that the Xe passes through the ND extremely quickly, taking around 0.02 ps as seen in the figure. The Xe exits the ND with a very high kinetic energy (23.2 keV), and also ejects a significant number of carbons (23 atoms). The combined kinetic energy of the ejected carbons is 15.0 keV, meaning that only 1.8 keV of the original Xe PKA energy is deposited into the ND. This results in an equilibrium ND temperature of around 2000 K as shown in Fig. 3(a). Since the temperature is slightly less than for the 2 keV case, the annealing effect which reduces the sp^3 fraction is also less significant, as can be seen in Fig. 3(b).

The behaviour at 6 keV is completely different to the higher and lower energy cases. Here, a much larger amount of kinetic energy is transferred to the ND. As shown in the sequence in the middle row of Fig. 4, the Xe exits the ND after 0.1 ps, but even at this stage there is already a significant amount of structural damage to the ND. The final kinetic energy of the Xe is 0.4 keV, while a total of 67 carbon atoms are ejected, with a combined kinetic energy of nearly 1 keV. In total, around 4.7 keV of kinetic energy is transferred to the ND, increasing the instantaneous temperature to well above the melting point as shown in Fig. 3(a). Note that the melting point is circa 4300–4500 K for EDIP, similar to experimental studies which find a value around 4500–5000 K with higher values more likely; see Savvatimskiy [26] for a rigorous discussion of the complexities of molten carbon. Even once the system has equilibrated, the temperature is extremely high, at just over 4000 K. At such a high temperature there is substantial conversion of sp^3 into sp^2 bonding in combination with some evaporation of atoms. As seen in Fig. 3(b), the sp^3 fraction is greatly reduced, and after 1 ps the majority of the tetrahedral bonding is lost. Due to the high temperature, running the 6 keV simulation beyond the 1 ps point drives further structural rearrangement. Figure 5 shows snapshots of the system up to a time of 80 ps, using color coding to indicate the hybridization. Note that the images in Fig. 5 are cross-sectional slices, whereas those in Fig. 4 show all atoms. After some tens of picoseconds, the ND has graphitized into a carbon onion structure, with spirals evident in cross-section. In the context of the implantation experiments, however, it is by no means apparent that such long annealing of an isolated ND is appropriate. We will return to this point later on by considering heat-loss paths which limit the amount of time the system spends at high temperature.

Ion implantation processes are sensitive to the impact param-

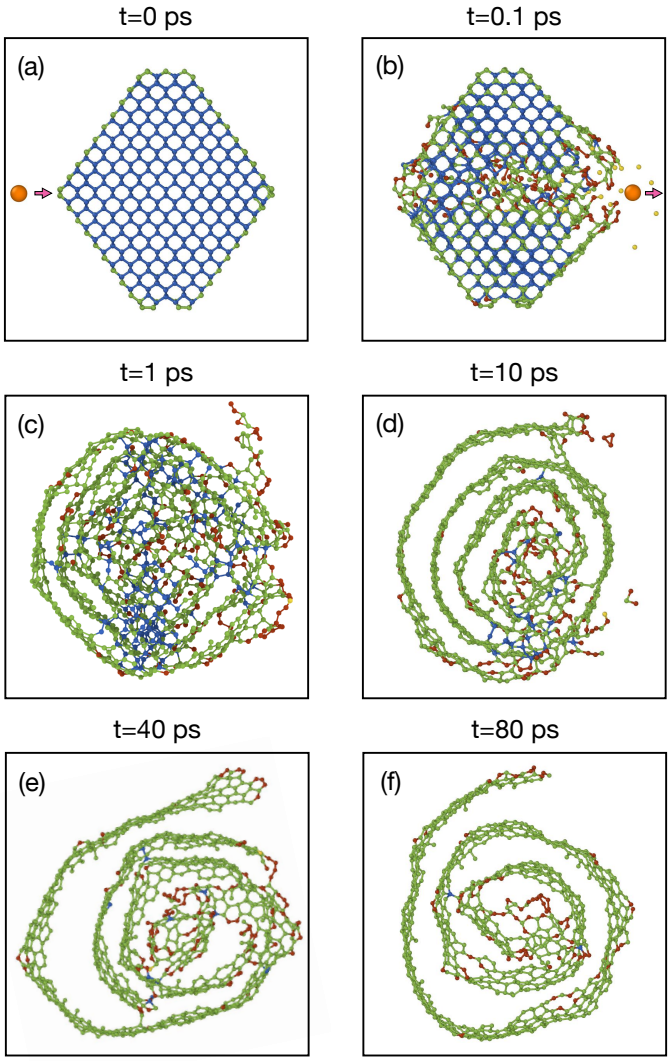

Figure 5: Cross-sectional snapshots (1 nm slices) for the time evolution of a 3.1 nm ND impacted by a 6 keV xenon ion. Note that this is the same impact as shown in Fig. 4, the difference being that the simulation continues up to 80 ps to show the effect of long-time annealing. Red, green and blue circles denote sp, sp^2 and sp^3 hybridization, respectively. Yellow atoms have just one neighbour and Xe is presented as a large orange circle.

eter of the primary collision and crystallographic orientation, and hence it is necessary to average over many different directions to collect accurate statistics. In the case of the 6 keV impact, for example, we found that for our 25 initial directions the final temperature of the ND varied from a low of 2520 K to a high of 4160 K. Similar variability was observed for all other quantities we extracted from the data. The merits of averaging are seen in Fig. 6 which shows the variation in the temperature, sp^3 fraction and number of carbon atoms ejected as a function of Xe energy. The error bars indicate the standard deviation, and even though the spread is substantial, the lines linking the mean values themselves are quite smooth, particularly for the temperature and sp^3 fraction. When the Xe energy is around 6 keV damage to the ND is maximal, with the sp^3 fraction [Fig. 6(b)] reduced to well under half its initial value and around 50 carbon atoms being ejected [Fig. 6(c)]. For higher Xe energies the nuclear stopping efficiency decreases significantly, leading to a lower residual temperature and much less damage (as measured by the sp^3 fraction and number of atoms ejected). At the highest energy considered, 40 keV, the effect of the Xe is very similar to that at 2 keV, consistent with the single impact sequences shown in Fig. 4.

The energy dependence of all three quantities in Fig. 6 are closely correlated, highlighting that the heating of the ND is the critical quantity that drives the damage process. When the ND temperature is 1000 K or so the sp^3 bonds are able to withstand the implantation due to the high melting point of diamond. However, when the temperature approaches several thousand degrees, sp^3 bonded atoms change to sp^2 and the ND begins

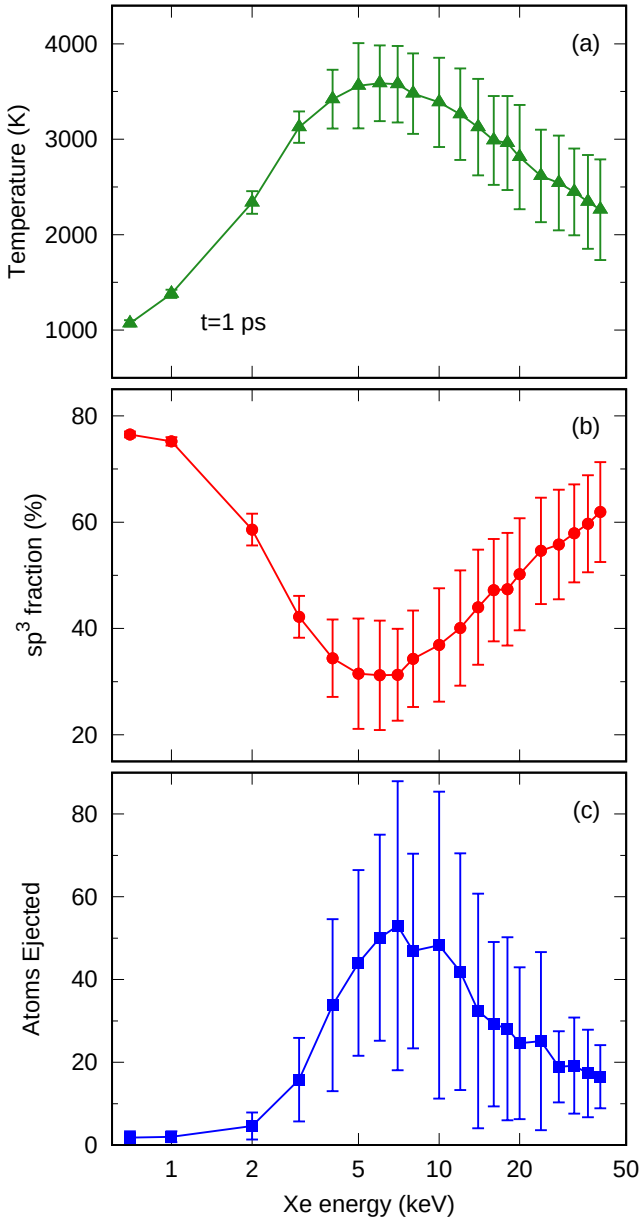

Figure 6: Effect of PKA energy for Xe implantation into a 3.1 nm diameter ND. All properties computed 1 ps after initiation of the PKA. (a) Cluster temperature, (b) sp^3 fraction, and (c) number of carbon atoms ejected.

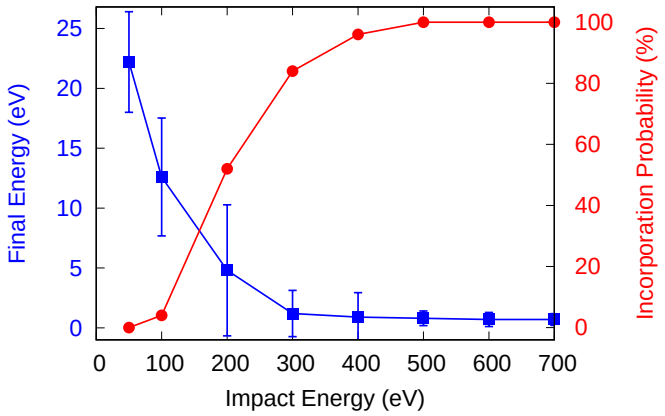

Figure 7: Final kinetic energy of the Xe atom (left-axis, blue squares), and implantation probability (right-axis, red circles) for 25 low-energy implantations onto a 3.1 nm ND. Error bars indicate one standard deviation.

to convert to a nested fullerene structure, or carbon onion, as shown in Fig. 8(a). The large number of sp^2 bonded atoms is seen in the large number of green atoms, consistent with the sp^3 fraction of ~30% at 6 keV as seen in Fig. 6.

It is instructive to examine more closely the low-energy regime in Fig. 6, since this is relevant to the ion-implantation experiments [6, 7] performed to interpret Xe release from meteoritic NDs. Figure 7 shows that for very low Xe energies (i.e. 50 eV) the Xe does not incorporate into the ND, and is reflected with around half its initial kinetic energy. For an incident energy of 200 eV there is a ~50% probability that the Xe will be incorporated, increasing to 100% at around 500 eV. For context, the experiments by Koscheev et al. [6] used an implantation energy of ~700 eV while those of Verchovsky et al. [7] used ~1000 eV and hence their experiments fall in a regime where the Xe is always implanted at least several atomic layers into the ND, but not with sufficient energy to pass through the ND. As a secondary observation, the modest energies used in their experiments implies only a small amount of heating as seen in Fig. 6; as a result there will be no annealing effect such as occurs for implantations in the vicinity of 6 keV. To clarify, these comments on the experimental implantation studies apply only to a single impact, while the experiments used doses of order 10^{15} ions/cm^2, corresponding to tens of ions per square-

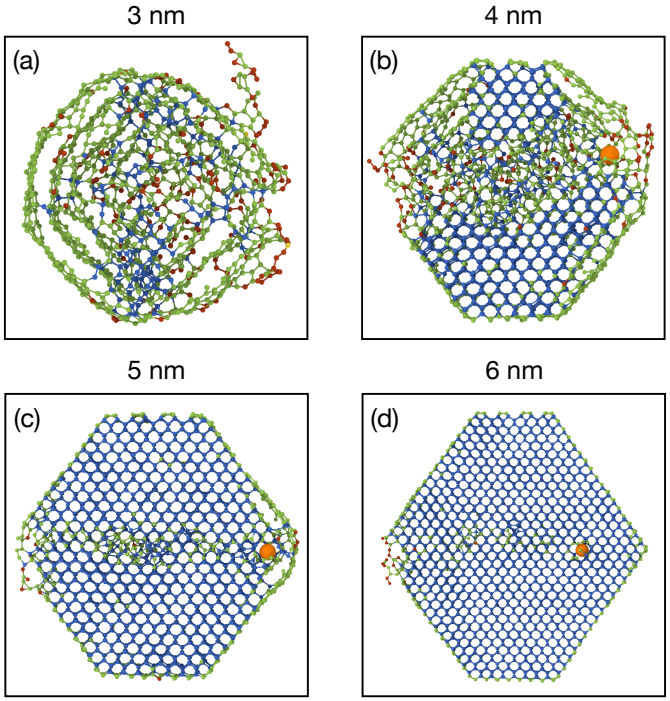

Figure 8: Cross-sectional snapshots (1 nm slices) showing how the size of the ND influences damage following implantation of a 6 keV Xe from the left of frame. All snapshots are 1 ps after impact. Color codings are the same as Fig. 5.

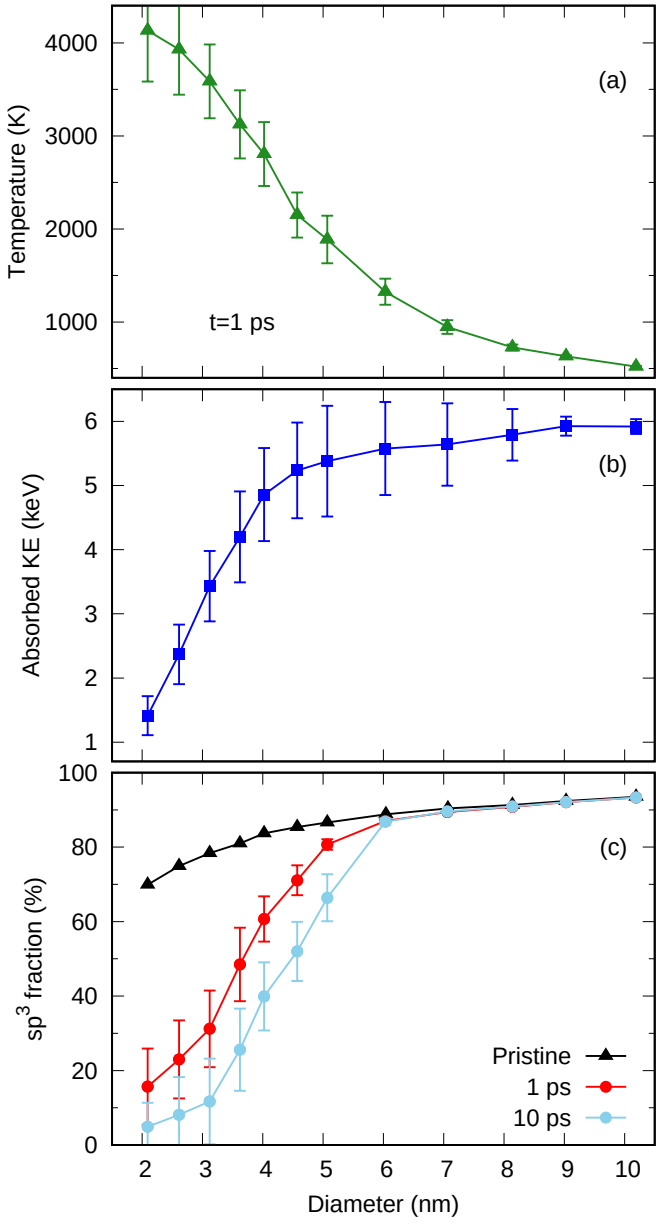

Figure 9: Effect of ND diameter for Xe implantation at a fixed PKA energy of 6 keV. All properties computed 1 ps after initiation of the PKA. (a) Cluster temperature, (b) sp^3 fraction, and (c) kinetic energy absorbed by the ND.

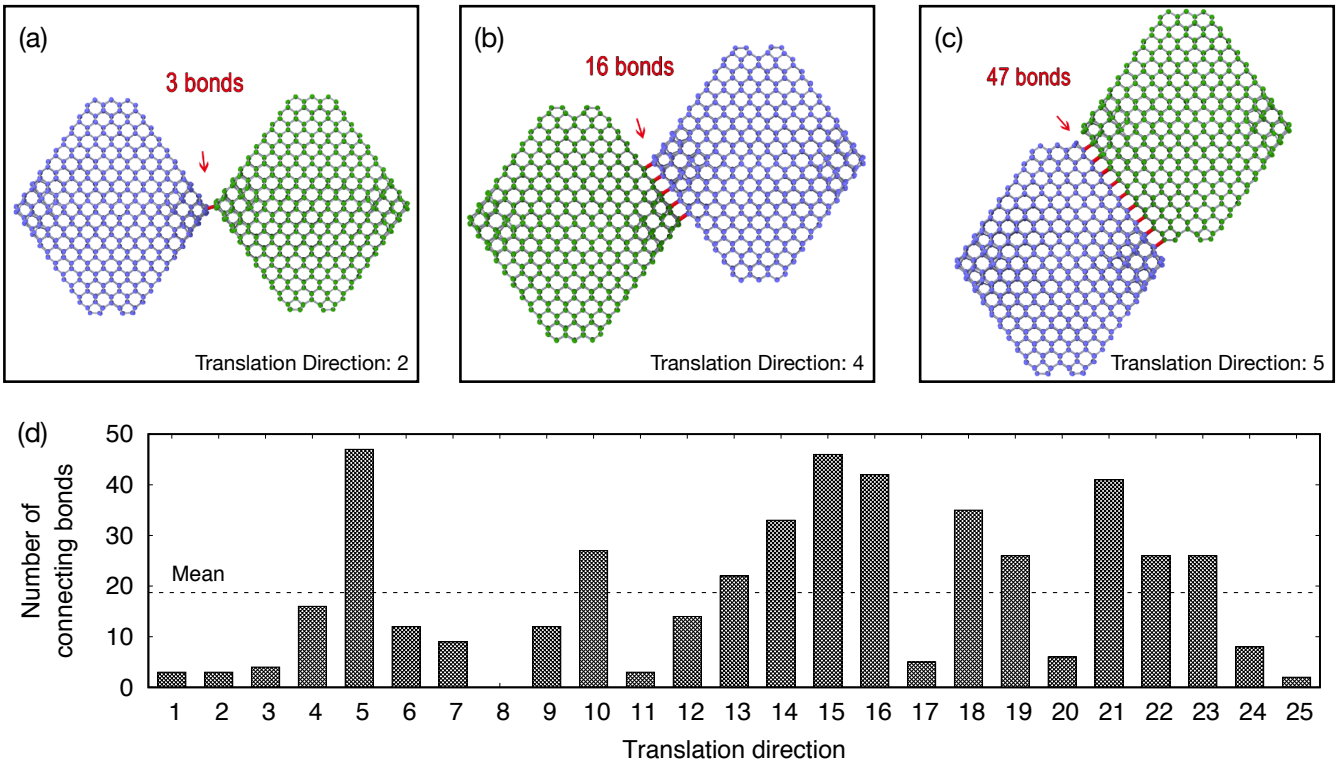

Figure 10: (a–c) Cross-sectional snapshots of three of the double-ND systems used to study the effect of thermal conduction. (d) Bar plot of the 25 different translation directions showing the number of bonds connecting the two NDs. Panel (a) shows the weakest thermal contact, comprising just 3 bonds. Panel (b) shows typical (average) thermal contact, with 16 bonds. Panel (c) shows the highest thermal contact, with 47 bonds. Connecting bonds are shown in red. Blue and green circles denote atoms and data for the primary and secondary ND, respectively.

nanometre. At these doses, individual NDs may be struck multiple times, leading to accumulated damage beyond that considered in the present simulations.

All of the data discussed to this point has been for a 3.1 nm diameter ND. To study the effect of varying the ND size, a series of calculations were performed using a 6 keV Xe and NDs ranging from 2.1 to 10.2 nm. Cross-sectional snapshots in Fig. 8 demonstrate that the size of the ND strongly influences the nature of the damage created by the Xe PKA. For larger diameters, such as the 5 and 6 nm NDs seen in panels (c and d), there is minimal disruption to the ND itself, and damage is concentrated along the trajectory of the Xe. In the case of the 6 nm ND, the residual damage consists of isolated point defects, much the same as for cascades in bulk diamond; see simulations by Buchan et al. [15]. For the 4 nm ND the damage caused by the Xe is much more substantial, with a wide damage track and graphitization on several (111) faces, while at 3 nm the ND is largely transformed into a carbon onion.

The size-dependence effect seen in Fig. 8 is explained by Fig. 9 which quantifies the temperature, sp^3 fraction and kinetic energy absorbed by the ND. Panel (a) shows that the cluster temperature falls off rapidly as the size of the ND increases; at 3 nm the average temperature after 1 ps is above 3500 K, close to the melting point of diamond. This high temperature explains the onionization behaviour seen in Fig. 8(a). For a 4 nm ND the temperature is around 700 K lower, reducing the extent of onionization but still sufficient to cause some structural rearrangement as seen in Fig. 8(b). For the 5 and 6 nm NDs the average temperature at 1 ps is circa 1900 and 1300 K, respectively, far below the diamond melting point, explaining why the damage tracks resemble those of bulk diamond.

Figure 9(b) quantifies the amount of kinetic energy which the Xe PKA deposits into the ND. This quantity is determined by summing the kinetic energy of all ejected particles (xenon plus carbons) and calculating the difference from the original value of 6 keV. The graph shows that the small NDs absorb only a small fraction of the total PKA energy, while for the large NDs the entire energy of the PKA is deposited into the ND. Even though more kinetic energy is absorbed by the large NDs, the final cluster temperature as shown in Fig. 9(a) monotonically decreases with increasing diameter due to the rapid increase in number of atoms with diameter. This demonstrates an important aspect of ion implantation into nanoparticles, namely that a small particle will only absorb a modest fraction of the PKA energy, but since a small particle contains few atoms, the resultant temperature increase is substantial.

Figure 9(c) quantifies the fraction of sp^3 bonds as a function of ND diameter; note that the maximum value (solid triangles) varies with diameter due to the changing surface-to-volume ratio. The loss of sp^3 bonding is particularly strong for the small NDs. After 1 ps, around 16% of the atoms in the 2 nm ND are sp^3 bonded, as compared to 70% sp^3 bonding in the original ND. As the diameter increases, the loss of sp^3 bonding gradually reduces, but remains significant in the 3–4 nm range. For

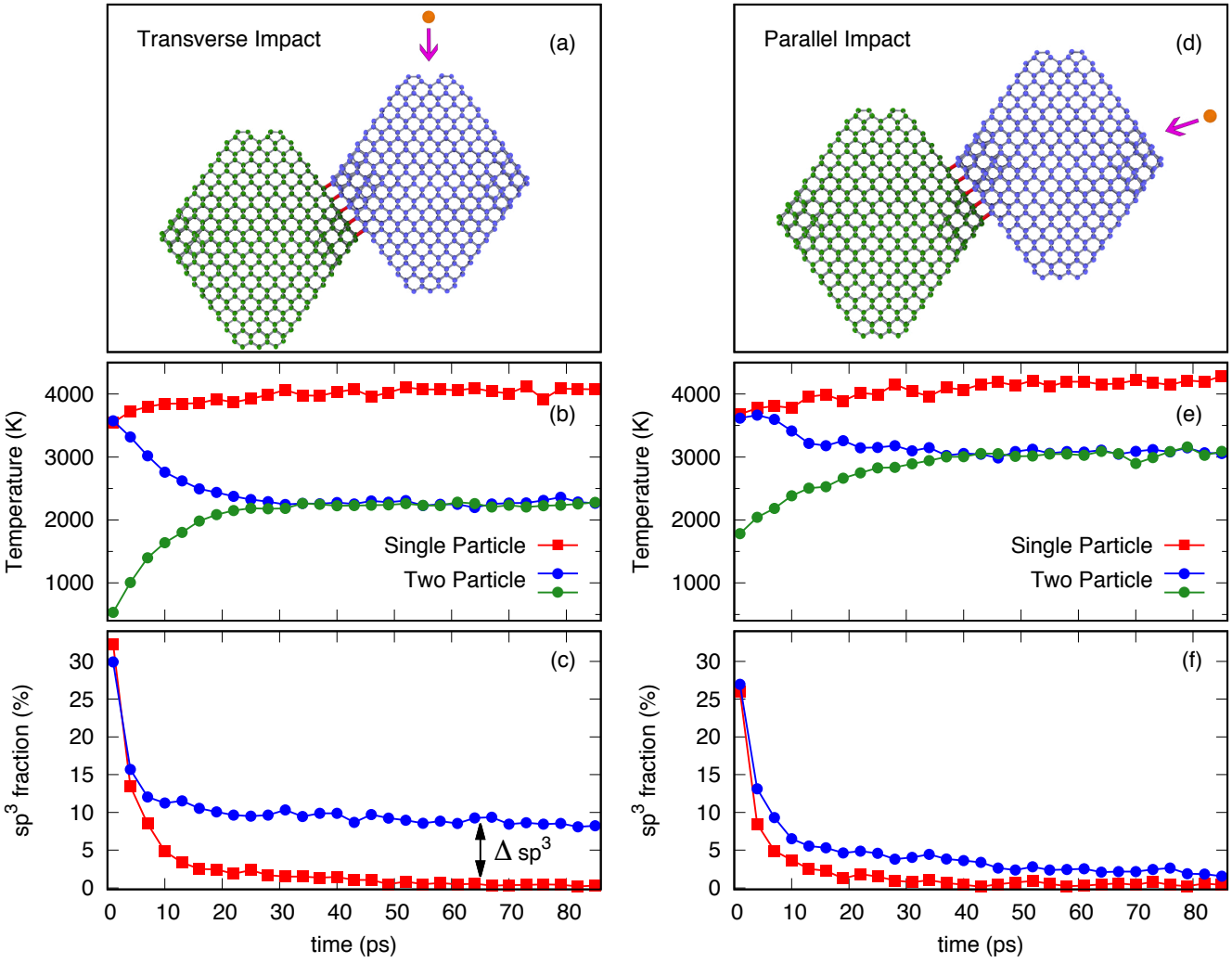

Figure 11: Time-evolution of temperature and sp^3 fraction for a 6 keV Xe impact into a double-ND system with average thermal contact [see Fig. 10(b)]. The first data point is 1 ps after initiation of the PKA, followed by data in 3 ps intervals. Panels (a–c) show the initial conditions and data for a transverse impact, in which the PKA direction is maximally orthogonal to the translation vector. Panels (d–f) show the same quantities for a parallel impact, in which the PKA direction is the same as the translation vector. Blue and green circles denote atoms and data for the primary and secondary ND, respectively. Red squares denote data for a single ND. The orange circle and pink arrow indicate the xenon atom and its initial direction, respectively.

NDs around 6 nm and above the sp^3 fraction is virtually unchanged due to the passage of the Xe.

The light-blue circles in Fig. 9(c) show the sp^3 fraction after 10 ps has elapsed. Since the NDs in these simulations are isolated, the residual thermal energy drives an annealing process which gradually graphitizes the smaller NDs. In the experimental situation however, thermal conduction with surrounding NDs will provide a heat-loss path, and hence the annealing process will not continue indefinitely. This raises the obvious question as to what simulation time should be used; thus far we have used 1 ps, but if thermal conduction is very rapid then a shorter simulation time should be used, and likewise, if thermal conduction is poor, then the NDs should be allowed to self-anneal for longer.

To address the question of thermal conduction between NDs, a second suite of calculations were performed in a system containing two identical NDs in varying degrees of thermal contact. The starting structure was the 3.1 nm ND, which was replicated and displaced along a vector correspond to one of the 25 Thomson points. The displacement was increased in small increments of 0.1 Å until the smallest bondlength in the entire double-ND system exceeded a threshold of 1.3 Å. The structure was then relaxed using steepest descent minimization. This process was repeated for the other 24 Thomson points, yielding a set of 25 double-ND systems exhibiting a wide range of thermal contact. The system with the weakest thermal contact is shown in Fig. 10(a), containing just 3 connecting bonds (red lines) connecting the two NDs. In contrast, the best thermal contact involved 47 connecting bonds as shown in Fig. 10(c). To determine a typical value of connections, we computed the number of connections for all 25 systems, as shown in the bar plot of Fig. 10. This shows that the average number of connections is around 18, for which the structure in Fig. 10(b) is a representative example.

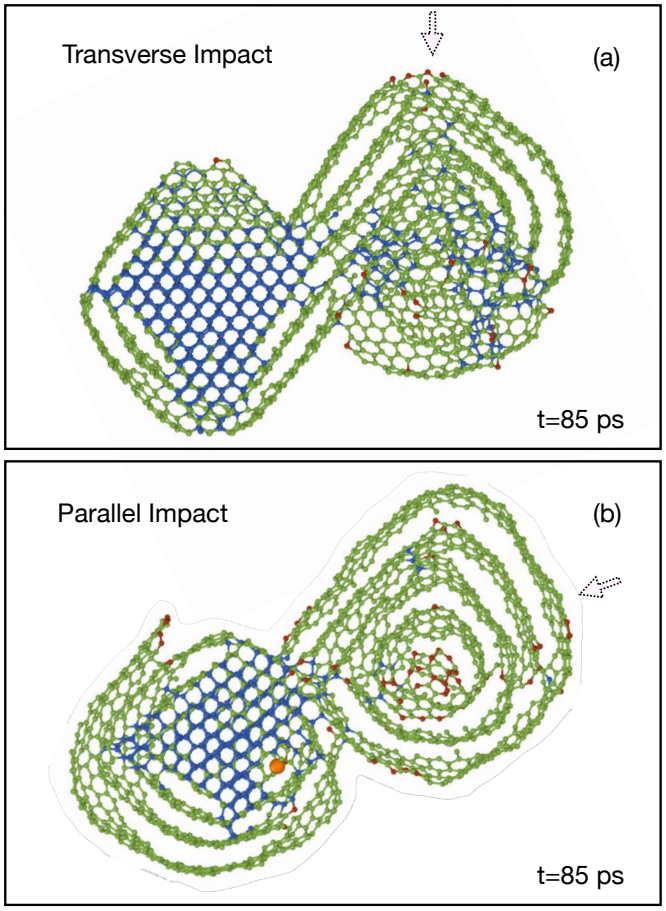

Figure 12: Cross-sectional snapshots (1 nm slices) showing the two double-ND systems seen in Fig. 11 after 85 ps of annealing. Color codings are the same as in Fig. 5. The orange circle and dotted arrow indicate the xenon PKA and its initial direction, respectively.

For all 25 double-ND systems, two 6 keV PKA simulations were performed. These simulations, which we refer to as either transverse or parallel, are shown in detail for the case of average thermal contact in Fig. 11. Snapshots of the two systems after 85 ps has elapsed are shown in Fig. 12. In the transverse impact case, the PKA direction is the Thomson point vector which is maximally orthogonal to the translation vector, while for the parallel impact case the PKA direction is the same as the translation vector. The blue and green circles in Fig. 11(b) show the temperature of the individual NDs as a function of time, using the same color scheme employed in panel (a) for the atoms. The heat-loss path provided by the secondary ND (green circles) has an obvious effect on the temperature of the primary ND, shown in blue. After approximately 30 ps the two NDs attain thermal equilibrium with each other, reaching a temperature of ~2250 K. The red squares in Fig. 11(b) show the exact same impact for a single-ND system in which there is no heat-loss path. In this case, the temperature of the ND is substantially higher, equilibrating at around 4000 K. The effect of this higher temperature on the sp^3 fraction of the primary-ND is shown in Fig. 11(c), with red and blue circles corresponding to the single- and double-ND systems, respectively. For the

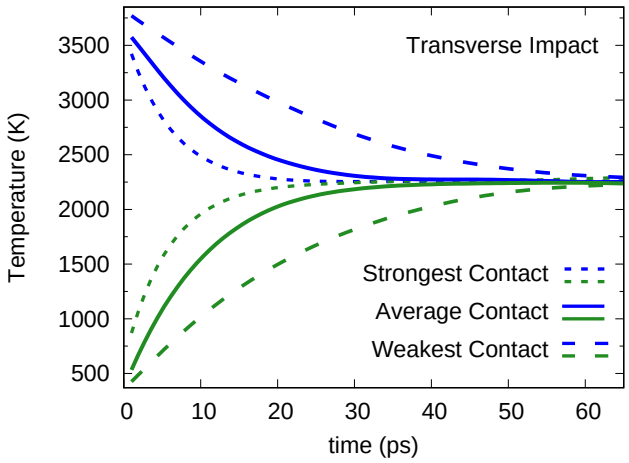

Figure 13: Time-evolution of temperature for a 6 keV transverse impact onto the double-ND systems corresponding to weakest thermal contact [Fig. 10(a)], average thermal contact [Fig. 10(b)] and strongest thermal contact [Fig. 10(c)]. The blue and green traces are decaying exponential fits to the raw data, and correspond to the primary and secondary ND, respectively.

single-ND case, all sp^3 bonding is lost and the ND transforms into a carbon onion, while for the double-ND around 8% of the sp^3 bonds persist [see primary ND in Fig. 12(a)]. While the effect of the heat-loss path is clearly apparent, it is important to recall that the original sp^3 fraction is 78%, and hence in both cases substantial modification of the ND occurs.

The parallel impact case shown in Fig. 11(d–f) demonstrates that the effect of thermal contact is influenced by the PKA direction. In this instance, the xenon atom is directed towards the centre of mass of both NDs, and this alignment means ballistic transfer of energy occurs between the primary and secondary NDs. As a result, the secondary ND is no longer just a heatsink as it was in the transverse impact case. Panel (e) shows that the equilibrium temperature is 3000 K, substantially higher than seen for the transverse impact, and much closer to the single impact data (red squares). As would be expected, the similarity in temperatures between the single- and double-ND systems means that the difference Δsp^3 in panel (f) is minimal. Due to the higher equilibrium temperature, the primary ND graphitizes completely into a carbon onion as seen in Fig. 12(b).

The equilibration between the primary and secondary ND seen in the non-ballistic, transverse impact data of Fig. 11(b) can be intuitively understood from a macroscopic perspective using Newton's law of heating/cooling. Both temperature profiles are well-fitted by decaying exponentials, with exponents of 9.0 and 8.4 ps^{-1} for the primary and secondary ND, respectively. The solid lines in Fig. 13 shows the corresponding fitted exponential curves, along with data for the cases of strongest and weakest thermal contact. The average decay constant for the strongest contact is 4.2 ps^{-1}, while for the weakest contact case it is 20 ps^{-1}. This data provides a timescale for the heat-loss path when NDs are in contact with one another. This situation is directly relevant to the *in situ* implantation/TEM experiments which motivated the present simulations. In the experiments, NDs were suspended in ethanol and deposited onto

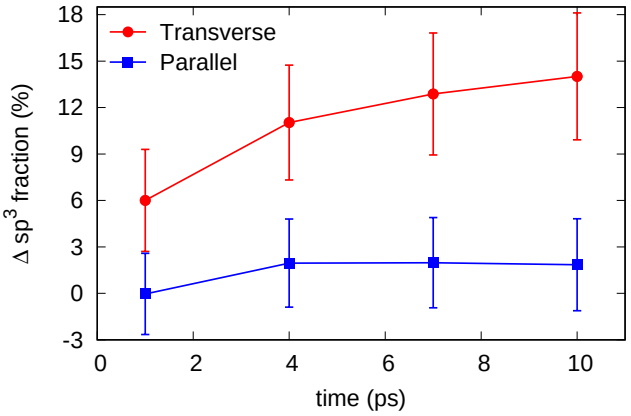

Figure 14: Effect of annealing time on the difference in sp^3 fraction between single- and double-ND systems for transverse (red circles) and parallel (blue squares) impacts. The sign convention is defined so that a positive difference means the double-ND value is higher. Data collected for all 25 of the translation directions (see Fig. 10) and the error bars indicate one standard deviation.

a holey carbon grid, producing an aggregate of NDs (see Fig. 1(a) in Ref. [8]) that provide a heat-loss path. Based on the simulation results, it is reasonable to propose that 1 ps of annealing is about right, while 10 ps is certainly too much, particularly since each ND will have some degree of thermal contact with several other NDs.

The effect of having too much annealing is illustrated in Fig. 14 which plots the quantity Δsp^3 (as defined in Fig. 11) as function of annealing time for transverse and parallel impacts. These two situations can be considered as the extrema, with a typical impact falling somewhere in-between. All data points are averages across 25 different translation directions and the errors denote one standard deviation. This sample is of sufficient size to display a clear trend in which overly long annealing times lead to significantly different sp^3 fractions for transverse impacts. In contrast, there is little effect for parallel impacts as the kinetic energy of the atoms ejected from the primary-ND is deposited into the secondary-ND; this increases the temperature of the secondary-ND, thereby reducing the temperature gradient along the heat-loss path.

4. Conclusion

In this paper, we showed how molecular dynamics simulation can be quantatively used to study implantation of xenon into nanodiamonds (NDs). Following on from our previous study [8], we provided detail on the key experimental/simulation result, namely, that a primary knock-on atom (PKA) energy around 6 keV provides maximal damage. We also detailed a pronounced size effect, showing that small NDs (below 3–4 nm diameter) are easily destroyed, losing many atoms and graphitizing those which remain. An important aspect of the damage process is the interplay between the amount of kinetic energy deposited in the ND, and the number of atoms in the ND itself. This energy transfer leads to thermal heating of the ND, with an effect seen only when the temperature approaches the rather high melting point of diamond. To assess the length of annealing that should be used in the simulations, we also studied a double-ND system in which two particles are touching with varying degrees of thermal contact. This mimics the heat bath that occurs in the experiment, and suggests an annealing time of one picosecond is reasonable.

The methodology developed here can be easily extended to describe a variety of similar topics. The most obvious is the implantation of noble gases into NDs, which is relevant to presolar studies where all of the noble gases are important. To extend the present work to elements other than xenon one simply needs to take Lennard-Jones parameters for noble gas interactions with carbon and bridge to the short-range ZBL expression as in Fig. 1. These parameters are easily obtainable due to the many studies of gas-adsorption onto carbon networks, and are conceptually straightforward due to the weak interactions between carbon and a noble gas atoms. Implantation involving other chemical species is also possible, but the interactions are less trivial due to the formation of formal chemical bonds. Beyond NDs, the noble gas implantation methodology can also be usefully applied to study ion-irradiation effects in a wide variety of different carbon nanoforms, such as graphene, graphene bilayers, fullerenes and nanotubes (see Ref. [27] for a summary of this field), as well as bulk materials such as glassy carbon, graphite and diamond.

Acknowledgements

This work was supported by Australian Research Council via Project FT120100924. Computational resources were provided by the Pawsey Supercomputing Centre with funding from the Australian Government and the Government of Western Australia.

References

[1] G. R. Huss, Meteoritic Nanodiamonds: Messengers from the Stars, Elements 1 (2005) 97–100. doi:10.2113/gselements.1.2.97.

[2] E. Anders, E. Zinner, Interstellar Grains in Primitive Meteorites: Diamond, Silicon Carbide, and Graphite, Meteoritics 28 (1993) 490–514. doi:10.1111/j.1945-5100.1993.tb00274.x.

[3] R. S. Lewis, T. Ming, J. F. Wacker, E. Anders, E. Steel, Interstellar diamonds in meteorites, Nature 326 (1987) 160–162. doi:10.1038/326160a0.

[4] A. B. Verchovsky, A. V. Fisenko, L. F. Semjonova, I. P. Wright, M. R. Lee, C. T. Pillinger, C, N, and Noble Gas Isotopes in Grain Size Separates of Presolar Diamonds from Efremovka, Science 281 (1998) 1165–1168. doi:10.1126/science.281.5380.1165.

[5] T. L. Daulton, D. D. Eisenhour, T. J. Bernatowicz, R. S. Lewis, P. R. Buseck, Genesis of presolar diamonds: Comparative high-resolution transmission electron microscopy study of meteoritic and terrestrial nanodiamonds, Geochimica et Cosmochimica Acta 60 (1996) 4853–4872. doi:10.1016/S0016-7037(96)00223-2.

[6] A. P. Koscheev, M. D. Gromov, R. K. Mohapatra, U. Ott, History of trace gases in presolar diamonds inferred from ion-implantation experiments, Nature 412 (2001) 615–617. doi:10.1038/35088009.

[7] A. B. Verchovsky, I. P. Wright, A. V. Fisenko, L. F. Semjonova, C. T. Pillinger, Ion Implantation into Presolar Diamonds: Experimental Simulation, Journal of Conference Abstracts 5 (2000) 1050. doi:10.1038/35088009.

[8] A. A. Shiryaev, J. A. Hinks, N. A. Marks, G. Greaves, F. J. Valencia, S. E. Donnelly, R. I. González, M. Kiwi, A. L. Trigub, E. M. Bringa, J. L. Fogg, I. I. Vlasov, Ion implantation in nanodiamonds: size effect and

energy dependence, Scientific Reports 8 (2018) 992. doi:10.1038/s41598-018-23434-y.

[9] N. A. Marks, Generalizing the environment-dependent interaction potential for carbon, Physical Review B 63 (2000) 2879–7. doi:10.1103/PhysRevB.63.035401.

[10] N. A. Marks, Modelling diamond-like carbon with the environment-dependent interaction potential, Journal of Physics: Condensed Matter 14 (2002) 2901–2927. doi:10.1088/0953-8984/14/11/308.

[11] C. de Tomas, I. Suarez-Martinez, N. A. Marks, Graphitization of amorphous carbons: A comparative study of interatomic potentials, Carbon 109 (2016) 681–693. doi:10.1016/j.carbon.2016.08.024.

[12] J. Ziegler, J. Biersack, U. Littmark, The Stopping and Range of Ions in Solids, Vol. 1, Pergamon, New York, 1985.

[13] H. J. Christie, M. Robinson, D. L. Roach, D. K. Ross, I. Suarez-Martinez, N. A. Marks, Simulating radiation damage cascades in graphite, Carbon 81 (2015) 105–114. doi:10.1016/j.carbon.2014.09.031.

[14] F. Vuković, J.-M. Leyssale, P. Aurel, N. A. Marks, Evolution of Threshold Displacement Energy in Irradiated Graphite, Physical Review Applied 10 (2018) 176. doi:10.1103/PhysRevApplied.10.064040.

[15] J. T. Buchan, M. Robinson, H. J. Christie, D. L. Roach, D. K. Ross, N. A. Marks, Molecular dynamics simulation of radiation damage cascades in diamond, Journal of Applied Physics 117 (2015) 245901–9. doi:10.1063/1.4922457.

[16] V. V. Simonyan, J. K. Johnson, A. Kuznetsova, J. T. Yates Jr., Molecular simulation of xenon adsorption on single-walled carbon nanotubes, The Journal of Chemical Physics 114 (2001) 4180–4185. doi:10.1063/1.1344234.

[17] N. A. Marks, M. Robinson, Variable timestep algorithm for molecular dynamics simulation of non-equilibrium processes, Nuclear Instruments and Methods in Physics Research, B 352 (2015) 3–8. doi:10.1016/j.nimb.2014.11.094.

[18] A. Stukowski, Visualization and analysis of atomistic simulation data with OVITO - the Open Visualization Tool, Modelling and Simulation in Materials Science and Engineering 18 (2010) 015012. doi:10.1088/0965-0393/18/8/085001.

[19] A. S. Barnard, P. Zapol, A model for the phase stability of arbitrary nanoparticles as a function of size and shape, The Journal of Chemical Physics 121 (2004) 4276–4283. doi:10.1063/1.1775770.

[20] A. Barnard, Diamond Nanoparticle Structure Set. v1. CSIRO. Data Collection (2014). doi:10.4225/08/546A9F79EC99C.

[21] Z. R. Dai, J. P. Bradley, D. J. Joswiak, D. E. Brownlee, H. G. M. Hill, M. J. Genge, Possible in situ formation of meteoritic nanodiamonds in the early Solar System, Nature 418 (2002) 157–159. doi:10.1038/nature00897.

[22] J. Thomson, On the structure of the atom: An investigation of the stability and periods of oscillation of a number of corpuscles arranged at equal intervals around the circumference of a circle; with application of the results to the theory of atomic structure, London, Edinburgh, Dublin Philosophical Magazine and Journal of Science 7 (1904) 237–265. doi:10.1080/14786440409463107.

[23] M. Robinson, N. A. Marks, G. R. Lumpkin, Sensitivity of the threshold displacement energy to temperature and time, Physical Review B 86 (2012) 134105–8. doi:10.1103/PhysRevB.86.134105.

[24] M. Robinson, N. A. Marks, K. R. Whittle, G. R. Lumpkin, Systematic calculation of threshold displacement energies: Case study in rutile, Physical Review B 85 (2012) 104105–11. doi:10.1103/PhysRevB.86.134105.

[25] M. Robinson, N. A. Marks, G. R. Lumpkin, Structural dependence of threshold displacement energies in rutile, anatase and brookite TiO2, Materials Chemistry and Physics 147 (2014) 311–318. doi:10.1016/j.matchemphys.2014.05.006.

[26] A. Savvatimskiy, Carbon at High Temperatures, Vol. 134, Springer Series in Materials Science, Switzerland, 2015. doi:10.1007/978-3-319-21350-7.

[27] A. V. Krasheninnikov, K. Nordlund, Ion and electron irradiation-induced effects in nanostructured materials, Journal of Applied Physics 107 (2010) 071301–71. doi:10.1063/1.3318261.